




## Tunable nonlinear excitonic optical response in biased bilayer graphene

M. F. C. Martins Quintela <sup>1,2,3,\*</sup>, N. M. R. Peres <sup>1,2,4</sup> and T. Garm Pedersen <sup>3</sup>

<sup>1</sup>*Department of Physics and Physics Center of Minho and Porto Universities (CF-UM-UP),  
Campus of Gualtar, 4710-057, Braga, Portugal*

<sup>2</sup>*International Iberian Nanotechnology Laboratory (INL), Av. Mestre José Veiga, 4715-330, Braga, Portugal*

<sup>3</sup>*Department of Materials and Production, Aalborg University, 9220 Aalborg Øst, Denmark*

<sup>4</sup>*POLIMA—Center for Polariton-driven Light-Matter Interactions,  
University of Southern Denmark, Campusvej 55, DK-5230 Odense M, Denmark*



(Received 9 May 2024; revised 8 August 2024; accepted 20 August 2024; published 29 August 2024)

Biased bilayer graphene (BBG) is an important system for studies of excitonic effects in graphene-based systems, with its easily tunable band gap. This band gap is governed by an external gate voltage, allowing one to tune the optical response of the system. In this paper, we study the excitonic linear and nonlinear optical responses of Bernal-stacked BBG as a function of the gate voltage, both for in-plane (IP) and out-of-plane (OOP) directions. Based on a semianalytical model of the electronic structure of BBG describing the influence of gate voltage on excitonic binding energies, we focus our discussion on both the IP and OOP excitonic responses. Both linear and second harmonic generation nonlinear responses are shown to be very sensitive to the gate voltage, as both the interband momentum matrix elements and the band gap of the system will vary greatly with bias potential.

DOI: [10.1103/PhysRevB.110.085433](https://doi.org/10.1103/PhysRevB.110.085433)

### I. INTRODUCTION

Since the first mechanical isolation of graphene [1], many different two-dimensional (2D) materials have been studied [2], such as hexagonal boron nitride (hBN) [3] and transition metal dichalcogenides (TMDs) [4]. This interest then recently transitioned into layered materials with broken vertical symmetry, which have been considered both from theoretical and experimental perspectives. These materials include, but are not limited to, buckled monolayers [5–8], Janus materials [9–13], heterobilayers and biased homobilayers [14–17]. In stark contrast to its monolayer counterpart, biased bilayer graphene (BBG) has a tunable gap which can be as large as 150 meV [14]. The magnitude of this band gap can be controlled via an external electric field and dielectric environment, and allows the formation of tunable excitons, which have already been both measured experimentally [18] and described theoretically [14,19–22].

As BBG presents an intrinsic out-of-plane (OOP) asymmetry due to the interlayer bias potential, one can directly study the effects of this asymmetry on the excitonic response. Tuning the interlayer bias potential, one can alter both the electronic structure of BBG and the interlayer asymmetry, probing the effects on both in-plane (IP) and OOP optical responses [23]. The probing of the OOP response, namely, the OOP nonlinearities, leads to additional degrees of freedom useful for vertical photonics structures [24,25], allowing for novel approaches in the design of ultrafast optical devices [12], such as nonlinear holograms [26], broadband

ultrafast frequency converters [27,28], miniaturized logic gates [29,30], among others. Furthermore, the presence of various nonzero tensor components which include nondiagonal components also provides a greater freedom when experimentally probing the optical response of BBG.

Recent theoretical works [31] have reviewed the effects of gate voltage on the free-carrier injection rate and shift current in AA- and AB- (Bernal-) stacked bilayer graphene, with many other theoretical works focusing on single-particle properties of bilayer graphene structures [32–37], especially when an interlayer twist angle is introduced [38–42]. However, and as in many layered materials, the optical response of BBG is dominated by excitons [43] and their effects are, therefore, fundamental in the study of the optical response of this material. In this paper, we focus on the effects of gate voltage on the excitonic optical response of AB-stacked bilayer graphene at  $T = 0$  K, considering both linear and SHG nonlinear response. As results for the linear IP response have been discussed previously in the literature [20,21], we focus mainly on the linear OOP response as well as the second harmonic generation (SHG) nonlinear response [44–47].

This paper is organized as follows: We begin, in Sec. II, by discussing the electronic structure and its dependence on the external gate voltage. This is then followed by the computation of the momentum and Berry connection matrix elements, both for IP and OOP directions. Knowing the momentum matrix elements, we compute the free-carrier linear response for both the full Hamiltonian and a reduced two-band model. This allows us to identify the frequency ranges where two bands are enough to describe the optical response of the system as a function of the gate voltage. Afterwards, in Sec. III, we proceed to the computation of the excitonic states through

\*Contact author: [mfcquintela@gmail.com](mailto:mfcquintela@gmail.com)

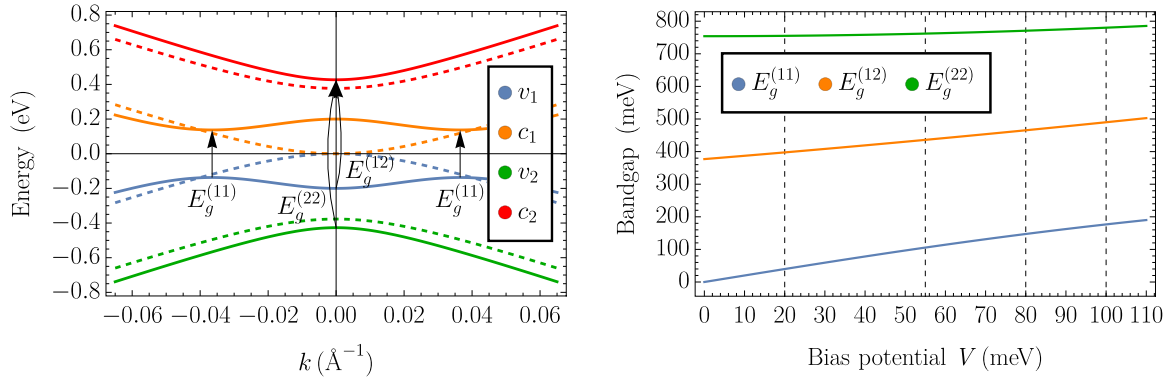


FIG. 1. (Left) Band structure of BBG with a large bias ( $V = 200$  meV) near the Dirac points. Colored dashed lines correspond to the band structure under zero external bias, vertical arrows represent the three direct band gaps. (Right) Evolution of the three distinct direct band gaps in BBG with increasing external bias near the Dirac points. Vertical dashed lines represent the four different values of  $V$  applied in numerical studies.

solving the Bethe-Salpeter equation. This involves an approximation of the effective screening length in the electron-hole electrostatic potential, followed by a discussion on the distinction between intralayer and interlayer phenomena. Finally, in Sec. IV, we compute the linear and SHG nonlinear excitonic optical response of BBG. After obtaining the IP and OOP optical selection rules for both linear and nonlinear responses, we discuss the effects of gate voltage, as well as the relative amplitudes of the different elements of the nonlinear conductivity tensor.

## II. SINGLE-PARTICLE BIASED BILAYER GRAPHENE HAMILTONIAN

In the basis  $\{|1, b\rangle, |2, b\rangle, |1, t\rangle, |2, t\rangle\}$ , where  $b$  ( $t$ ) denotes the bottom (top) layer and 1 and 2 denote the different sublattices in each layer, the Hamiltonian of Bernal-stacked BBG [48] in the Dirac approximation around the Dirac points ( $K_x, \tau K_y$ ), with  $\tau = \pm 1$  the valley index, is given by

$$\mathcal{H} = \begin{pmatrix} V & -\gamma_0 f & 0 & -i\gamma_3 f^* \\ -\gamma_0 f^* & V & \gamma_z & 0 \\ 0 & \gamma_z & -V & -\gamma_0 f \\ i\gamma_3 f & 0 & -\gamma_0 f^* & -V \end{pmatrix}, \quad (1)$$

where  $V$  is the bias potential applied to the bilayer system,  $\gamma_0 = 3.12$  eV is the intralayer nearest-neighbor hopping parameter, and the interlayer parameters  $\gamma_z = 0.377$  eV (interlayer direct vertical coupling), and  $\gamma_3 = 0.377$  eV (skew coupling parameter). Restricting our analysis to the Dirac cones  $K, K'$ , we consider  $\mathbf{k}$  measured from the Dirac points and write

$$f(\mathbf{k}) \approx \frac{\sqrt{3}}{2} a(k_x - i\tau k_y)$$

with  $\hbar v_F = \frac{\sqrt{3}}{2} a\gamma_0$  the Fermi velocity, the polar angle of  $\mathbf{k}$  defined as  $\theta = \tan^{-1}(\frac{k_y}{k_x})$ , and  $a = 2.46$  Å the lattice parameter. The interlayer bias potential  $2V$  corresponds to placing the system in an electric field  $\frac{2V}{ed}$ , with  $d$  the interlayer separation. In this paper we will mainly consider  $V = 55$  meV as it is at this bias that the dominant peak in the IP linear response matches with recent experimental results [18].

The band structure under the Dirac approximation is given by

$$E_{\lambda\eta} = \lambda\sqrt{\hbar^2 v_F^2 k^2 + V^2 + \frac{1}{2}\gamma_z^2 + (2\eta - 3)\Lambda},$$

$$\Lambda = \sqrt{\frac{1}{4}\gamma_z^4 + \hbar^2 v_F^2 k^2 (4V^2 + \gamma_z^2)}, \quad (2)$$

where  $\lambda = \pm 1$  represents the conduction and valence bands [ $\lambda = +1$  will be conduction (c) bands,  $\lambda = -1$  valence (v) bands], and  $\eta = 1, 2$  identifies the band closest ( $\eta = 1$ ) and furthest away ( $\eta = 2$ ) from the band gap. Direct substitution of  $\eta = 1, 2$  into Eq. (2) leads to a factor of  $\pm 1$ , as expected for the band structure of this system. This band structure is presented in Fig. 1. Focusing on direct band gaps, we write the generic band gap as

$$E_g^{(\eta, \eta')} = E_{c_\eta} - E_{v_{\eta'}}. \quad (3)$$

Due to the nature of the BBG band structure, the minimum bandgap between the two  $\eta = 1$  bands will not occur at  $k = 0$  (see left panel of Fig. 1), instead occurring at

$$k = \sqrt{2} \frac{V}{\hbar v_F} \sqrt{\frac{2V^2 + \gamma_z^2}{4V^2 + \gamma_z^2}} \quad (4)$$

measured from the Dirac points. For instance,

$$E_g^{(11)} = \frac{2V\gamma_z}{\sqrt{4V^2 + \gamma_z^2}} \approx 106 \text{ meV} \quad (5)$$

for the considered bias potential  $V = 55$  meV. The two larger direct band gaps, namely,  $E_g^{(12)}$  and  $E_g^{(22)}$ , will occur at  $k = 0$  and are significantly larger. For  $V = 55$  meV, these take the values

$$E_g^{(12)} = V + \sqrt{V^2 + \gamma_z^2} \approx 436 \text{ meV},$$

$$E_g^{(22)} = 2\sqrt{V^2 + \gamma_z^2} \approx 762 \text{ meV}, \quad (6)$$

and  $E_g^{(21)} = E_g^{(12)}$ . The three distinct band gaps are plotted in the right panel of Fig. 1 for external bias between 0 and 110 meV. The large difference between the three band gaps suggests that, as we will see ahead, the two  $\eta = 1$  bands will dominate the low-energy response of the system.

### A. In-plane matrix elements

For simplicity, we will discard the contributions from skew coupling to the eigenvectors, considering it instead as a perturbation when computing dipole matrix elements. In a compact notation, we define the normalized eigenvectors for future computations as

$$|\lambda_\eta(\mathbf{k})\rangle = \begin{bmatrix} e^{-2i\tau\theta} \alpha_{1,\lambda_\eta}(k) \\ e^{-i\tau\theta} \alpha_{2,\lambda_\eta}(k) \\ e^{-i\tau\theta} \alpha_{3,\lambda_\eta}(k) \\ \alpha_{4,\lambda_\eta}(k) \end{bmatrix}. \quad (7)$$

This gauge choice will carry a pseudospin [14,20,49–52] factor of  $m_s = -2$  in the  $\tau = 1$  valley. For compactness in the expressions for the momentum matrix elements and Berry connections, the  $k$  dependence in the eigenvector components will be suppressed.

To compute the IP interband momentum matrix elements, chosen without loss of generality in the  $x$  direction, we must analyze

$$P_{v_\eta c_{\eta'} \mathbf{k}}^x = \frac{m_0}{\hbar} \left\langle v_\eta \left| \frac{\partial \mathcal{H}}{\partial k_x} \right| c_{\eta'} \right\rangle, \quad (8)$$

where  $m_0$  is the free-electron mass. The operator  $\frac{\partial \mathcal{H}}{\partial k_x}$  can be readily computed and is given by

$$\frac{\partial \mathcal{H}}{\partial k_x} = \begin{pmatrix} 0 & -\hbar v_F & 0 & -i \frac{\gamma_3}{\gamma_0} \hbar v_F \\ -\hbar v_F & 0 & 0 & 0 \\ 0 & 0 & 0 & -\hbar v_F \\ i \frac{\gamma_3}{\gamma_0} \hbar v_F & 0 & -\hbar v_F & 0 \end{pmatrix}.$$

Yet, obtaining the matrix elements taking into account skew coupling due to finite  $\gamma_3$  in the eigenvectors becomes extremely unwieldy. As a consequence, we consider an approximation where  $\gamma_3$  is taken as a small perturbation to the Dirac BBG system and, therefore, its only effect will be introducing additional terms in the momentum matrix elements proportional to  $\frac{\gamma_3}{\gamma_0} \hbar v_F$ , as presented in  $\frac{\partial \mathcal{H}}{\partial k_x}$ . This follows the approach previously outlined in a similar study of the linear response of BBG [20], where experimental results [18] were accurately predicted under this same perturbative approach. This also means that skew coupling will play no part in the calculation of Berry connections, as it is only dependent on the eigenvectors defined in Eq. (7).

Focusing only on the  $\eta = 1$  bands, the exciton momentum matrix element will be given explicitly as

$$P_{v_\eta c_{\eta'} \mathbf{k}}^x = m_0 v_F \left[ e^{i\tau\theta} (\alpha_{1,v_\eta}^* \alpha_{2,c_{\eta'}} + \alpha_{3,v_\eta}^* \alpha_{4,c_{\eta'}}) + e^{-i\tau\theta} (\alpha_{2,v_\eta}^* \alpha_{1,c_{\eta'}} + \alpha_{4,v_\eta}^* \alpha_{3,c_{\eta'}}) - i \frac{\gamma_3}{\gamma_0} (e^{2i\tau\theta} \alpha_{1,v_\eta}^* \alpha_{4,c_{\eta'}} - e^{-2i\tau\theta} \alpha_{4,v_\eta}^* \alpha_{1,c_{\eta'}}) \right]. \quad (9)$$

In this form, it is also clear from the phase factors that, upon multiplication by the conjugate and angular integration, the lowest contribution from skew coupling to the linear response will be quadratic in  $|\gamma_3/\gamma_0| \approx 0.1$ . As  $|\gamma_3/\gamma_0| \ll 1$ , we will keep only the dominant term in each expansion. The validity of this perturbative approach has also been checked against a full tight-binding numerical calculation.

Comparing both the single-particle Hamiltonian as in Eq. (1) and the momentum matrix element as given in Eq. (9) against those used in Ref. [20], one can see that Ref. [20] is missing the  $i$  factor in the skew coupling contribution for both the Hamiltonian and the momentum matrix element. Although the lack of this term is of no consequence for the linear response discussed in Ref. [20] due to the proportionality to  $|\gamma_3/\gamma_0|^2$ , this factor is of importance for the IP nonlinear response as it will be clear when the excitonic matrix elements are discussed.

A different contribution, namely, trigonal warping, consists of considering the quadratic term in the series expansion of  $f$ , leading to [53]

$$f(\mathbf{k}) \approx \frac{\sqrt{3}a}{2} [(k_x - i\tau k_y) + i\zeta_{\text{TW}} a (k_x - i\tau k_y)^2], \quad (10)$$

where  $\zeta_{\text{TW}} = \frac{\sqrt{3}}{12}$  is a fixed numerical factor resulting from the series expansion of  $f$ . Careful analysis of the effects of this quadratic term on the momentum matrix elements via Eq. (8) reveals that the phase factor associated will be  $e^{\pm 2i\tau\theta}$ , identical to the contribution from skew coupling in Eq. (9). Furthermore, upon computation of the excitonic matrix elements, this quadratic correction proves to be negligible when compared against that originating from skew coupling and, therefore, it will be ignored.

In the  $k_x$  direction, the matrix elements of the Berry connection between bands  $n_\eta$  and  $m_\eta$  read as

$$\Omega_{n_\eta m_\eta \mathbf{k}}^x = i \langle n_\eta | \frac{\partial}{\partial k_x} | m_\eta \rangle. \quad (11)$$

The exact form of the Berry connection will be needed when computing generalized derivatives [54] and  $\Omega_{c_\eta c_{\eta'} \mathbf{k}}^x$  will be given in terms of the eigenvector components as

$$\begin{aligned} \Omega_{c_\eta c_{\eta'} \mathbf{k}}^x &= i \cos \theta \left( \alpha_{1,c_\eta}^* \frac{\partial \alpha_{1,c_{\eta'}}}{\partial k} + \alpha_{2,c_\eta}^* \frac{\partial \alpha_{3,c_{\eta'}}}{\partial k} \right. \\ &\quad \left. + \alpha_{3,c_\eta}^* \frac{\partial \alpha_{3,c_{\eta'}}}{\partial k} + \alpha_{4,c_\eta}^* \frac{\partial \alpha_{4,c_{\eta'}}}{\partial k} \right) \\ &\quad - \frac{\tau}{k} \sin \theta (2\alpha_{1,c_\eta}^* \alpha_{1,c_{\eta'}} + \alpha_{2,c_\eta}^* \alpha_{1,c_{\eta'}} + \alpha_{3,c_\eta}^* \alpha_{3,c_{\eta'}}), \end{aligned} \quad (12)$$

and  $\Omega_{v_\eta v_{\eta'} \mathbf{k}}^x$  will be defined analogously for the valence bands.

### B. Out-of-plane matrix elements

Before computing the single-particle linear optical response, we will discuss the OOP momentum and Berry connection. To this end, we begin by defining the matrix elements of  $z$  from the extension of  $\frac{d}{2} \sigma_z$  [55] to a bilayer system, with  $\sigma_z$  the diagonal Pauli matrix, as

$$z_{n_\eta m_\eta \mathbf{k}} = \frac{1}{2} \langle n_\eta | \text{diag}[d, d, -d, -d] | m_\eta \rangle. \quad (13)$$

The interlayer separation  $d$  has been previously discussed in the literature [56–59], with reported values for  $d \approx 3.46 \text{ \AA}$ . The momentum matrix element then reads as

$$P_{v_\eta c_{\eta'} \mathbf{k}}^z = \frac{m_0}{i\hbar} E_{c_{\eta'} v_\eta \mathbf{k}} z_{v_\eta c_{\eta'} \mathbf{k}}. \quad (14)$$

Explicitly computing  $z_{v_\eta c_{\eta'} \mathbf{k}}$ , we obtain

$$P_{v_\eta c_{\eta'} \mathbf{k}}^z = \frac{m_0 d}{2i\hbar} E_{c_{\eta'} v_\eta \mathbf{k}} [\alpha_{1, v_\eta}^* \alpha_{1, c_{\eta'}} + \alpha_{2, v_\eta}^* \alpha_{2, c_{\eta'}} - \alpha_{3, v_\eta}^* \alpha_{3, c_{\eta'}} - \alpha_{4, v_\eta}^* \alpha_{4, c_{\eta'}}]. \quad (15)$$

For the nonlinear response, we must also compute the matrix elements  $z_{c_\eta c_{\eta'} \mathbf{k}}$ ,  $z_{v_\eta v_{\eta'} \mathbf{k}}$ . Similarly to  $z_{v_\eta c_{\eta'} \mathbf{k}}$ , we write these in terms of the radial components of the eigenvectors as

$$z_{c_\eta c_{\eta'} \mathbf{k}} = \frac{d}{2} [\alpha_{1, c_\eta}^* \alpha_{1, c_{\eta'}} + \alpha_{2, c_\eta}^* \alpha_{2, c_{\eta'}} - \alpha_{3, c_\eta}^* \alpha_{3, c_{\eta'}} - \alpha_{4, c_\eta}^* \alpha_{4, c_{\eta'}}],$$

and analogous for  $z_{v_\eta v_{\eta'} \mathbf{k}}$ . Hence, we obtain the Berry connection as [54]

$$\Omega_{c_\eta c_{\eta'} \mathbf{k}}^z - \Omega_{v_\eta v_{\eta'} \mathbf{k}}^z = z_{c_\eta c_{\eta'} \mathbf{k}} - z_{v_\eta v_{\eta'} \mathbf{k}}. \quad (16)$$

### C. Single-particle linear optical response

In a clean semiconductor at zero temperature, the diagonal optical response reads as [54,60–63]

$$\sigma_{\beta\beta}(\omega) = \frac{e^2 \hbar^2 \omega}{i\pi^2 m_0^2} \sum_{c,v} \int \frac{|P_{c v \mathbf{k}}^\beta|^2}{E_{c v \mathbf{k}} (E_{c v \mathbf{k}}^2 - \hbar^2 \omega^2)} d^2 \mathbf{k}, \quad (17)$$

where  $\sum_{c,v}$  sums over all conduction and valence bands. Within the two-band approximation, the sum over valence and conduction bands is dropped. With the expansion near the Dirac cones, integration will now be over the infinite Dirac cones and a sum over valleys must also be made.

Inspecting Eq. (9), one sees that the angular integration is trivial. Although the radial integration proves much more complicated, one can easily perform it numerically by employing a simple numerical quadrature in a tangent grid  $q = \tan(x\frac{\pi}{2})$  with 1500 points  $x \in [0, 1]$ , following the procedure already outlined several times in the literature, namely, in Refs. [20,64–66]. Introducing a broadening parameter via the transformation  $\hbar\omega \rightarrow \hbar\omega + i\hbar\Gamma$  with  $\hbar\Gamma = 5$  meV, we obtain both the free-carrier IP (top) and OOP (bottom) linear optical response as depicted in Fig. 2, with  $\sigma_0 = e^2/4\hbar$ .

While the free-carrier response can be easily computed for the full four-band system, the same is not true when one wishes to obtain the excitonic response. The four possible combinations of valence and conduction bands would lead to a drastic increase in the computational complexity of both solving the Bethe-Salpeter equation and of obtaining the excitonic momentum matrix elements [20,52,67]. Hence, it becomes crucial to reduce the system to a two-band problem when one wants to consider its excitonic properties. As seen in Fig. 2, and as expected from the large separation of the higher-energy bands, we observe minimal differences in the real part of the linear response between the four- and two-band responses if  $\hbar\omega \lesssim 400$  meV, consistent with previous results [20,66]. Hence, we will consider only the two  $\eta = 1$  bands from this point onward. This will, however, introduce issues when the imaginary part of  $\sigma$  is relevant (i.e., when considering the magnitude of the various components of the conductivity tensor). This is because, while the real part of  $\sigma$  only gets contributions from transitions resonant with  $\hbar\omega$  (i.e., remote bands do not contribute substantially), the imaginary part, in contrast, presents contributions from remote bands

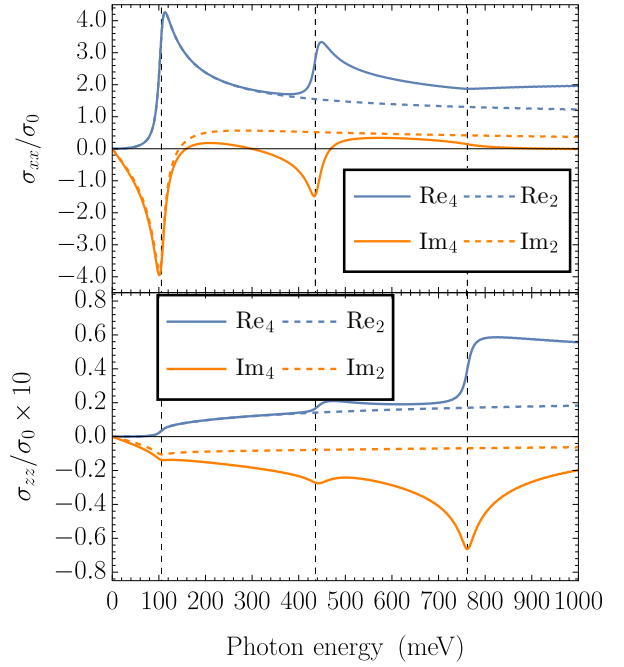


FIG. 2. Comparison between full four-band calculation and calculation with only the two lowest bands of both IP (top) and OOP (bottom) free-carrier linear optical response for biased bilayer graphene with a bias potential  $V = 55$  meV and broadening  $\hbar\Gamma = 5$  meV. Real part represented in blue, denoted  $\text{Re}_n$ , and imaginary part in orange, denoted  $\text{Im}_n$ , for the  $n$ -band calculation. Vertical dashed lines represent the various band gaps of the system, from left to right  $E_g^{(11)}$ ,  $E_g^{(12)}$ ,  $E_g^{(22)}$ .

as it behaves as  $1/(\omega - E_{nm})$ . Therefore, while a two-band approximation can accurately model the real part of  $\sigma$  for low frequencies, it quickly fails for the imaginary part as seen in Fig. 2. Additionally, as only the two  $\eta = 1$  bands have an effect on the real part of the conductivity up to  $\hbar\omega \approx E_g^{(12)}$  (for  $V = 55$  meV, up to  $\hbar\omega \approx 400$  meV), one can expect minimal effects on the real part of the SHG nonlinear conductivity up to  $\hbar\omega \approx E_g^{(12)}/2$ . The imaginary part will, however, be significantly different from the four-band calculation much earlier due to both the longer range of the peaks in the imaginary part and the presence of resonances at  $2\hbar\omega$ .

### III. BETHE-SALPETER EQUATION

As discussed in the preceding section, we will focus on the dominant response from the two bands closest to the band gap  $c_1, v_1$ , which we denote  $c, v$ . Hence, we are only interested in the eigenvalues  $E_{c/v}$  and their respective eigenvectors  $|c/v\rangle$ . Additionally, we will ignore contributions to eigenvectors from the skew coupling parameter, as this will allow us to transform the Bethe-Salpeter equation (BSE) from a 2D integral equation into a 1D integral equation.

Before discussing the excitonic conductivity, we must first compute the excitonic states. To compute the excitonic wave functions and binding energies, we will solve the

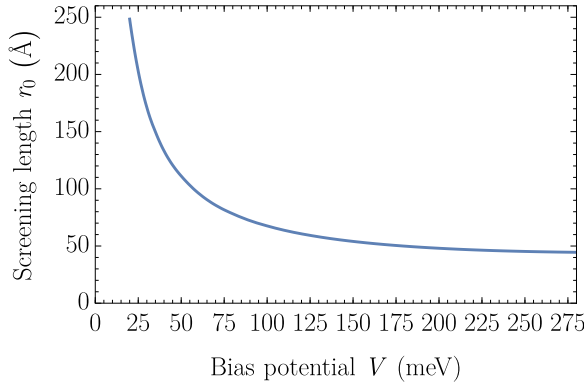


FIG. 3. Evolution of the effective screening length  $r_0$  as a function of external bias  $V$ , as computed in a dipole approximation via Eq. (20).

BSE [51,53,63,68,69], given in momentum space by

$$E_n \psi_{cv\mathbf{k}}^{(n)} = E_{cv\mathbf{k}} \psi_{cv\mathbf{k}}^{(n)} + \sum_{\mathbf{q}} V(|\mathbf{k} - \mathbf{q}|) \langle c_{\mathbf{k}} | c_{\mathbf{q}} \rangle \langle v_{\mathbf{q}} | v_{\mathbf{k}} \rangle \psi_{cv\mathbf{q}}^{(n)} \quad (18)$$

where  $E_n$  is the exciton energy of state  $n$ ,  $V(k)$  is the attractive electrostatic potential coupling the electron and the hole, and  $\psi_{cv\mathbf{k}}^{(n)}$  is the wave function of the exciton. For our system, we consider  $V(k)$  to be the Rytova-Keldysh potential [70,71],

$$E_n f_{cv\mathbf{k}}^{(n)} = E_{cv\mathbf{k}} f_{cv\mathbf{k}}^{(n)} + \frac{1}{4\pi^2} \sum_{\ell=-2}^2 \int_0^{+\infty} \int_0^{2\pi} V(|\mathbf{k} - \mathbf{q}|) \mathcal{A}_{\ell}(k, q) e^{i\ell\tau\varphi} f_{cv\mathbf{q}}^{(n)} e^{i\ell_n\varphi} d\varphi q d\mathbf{q}, \quad (22)$$

where  $\varphi = \theta_q - \theta_k$ . The radial component of the form factor can then be written by analyzing the expansion of  $\langle c_{\mathbf{k}} | c_{\mathbf{q}} \rangle \langle v_{\mathbf{q}} | v_{\mathbf{k}} \rangle$  as in terms of the  $\ell$  factors in the complex exponential of the form  $e^{i\ell\tau\varphi}$  in Eq. (22). This then fixes the ranges on the sum over  $\ell$  present in Eq. (22). For a monolayer system, the form factor reads as, in a somewhat abusive notation,

$$\mathcal{A}_{\ell}(k, q) e^{i\ell\tau\varphi} = \langle c_{\mathbf{k}} | c_{\mathbf{q}} \rangle \langle v_{\mathbf{q}} | v_{\mathbf{k}} \rangle, \quad (23)$$

identical to what is present in Eq. (18). However, when one wishes to consider a bilayer system where there is a distinction between interlayer and intralayer phenomena, one must compute the form factor more carefully. Recalling the eigenvectors from Eq. (7), separated into top- and bottom-layer components as

$$|\lambda\rangle = \begin{bmatrix} |\lambda^t\rangle \\ |\lambda^b\rangle \end{bmatrix}, \quad (24)$$

we explicitly introduce a distinction between intralayer and interlayer interactions by writing the form factor as

$$\begin{aligned} \mathcal{A}_{\ell}(k, q) e^{i\ell\tau\varphi} &= \langle c_{\mathbf{k}}^t | c_{\mathbf{q}}^t \rangle \langle v_{\mathbf{q}}^t | v_{\mathbf{k}}^t \rangle + \langle c_{\mathbf{k}}^b | c_{\mathbf{q}}^b \rangle \langle v_{\mathbf{q}}^b | v_{\mathbf{k}}^b \rangle \\ &+ e^{-d|\mathbf{k}-\mathbf{q}|} [\langle c_{\mathbf{k}}^t | c_{\mathbf{q}}^b \rangle \langle v_{\mathbf{q}}^b | v_{\mathbf{k}}^t \rangle + \langle c_{\mathbf{k}}^b | c_{\mathbf{q}}^t \rangle \langle v_{\mathbf{q}}^t | v_{\mathbf{k}}^b \rangle], \end{aligned} \quad (25)$$

where  $d \approx 3.46 \text{ \AA}$  is the interlayer separation between the two graphene layers [56–59]. The extra  $e^{-d|\mathbf{k}-\mathbf{q}|}$  factor present in

given in momentum space by

$$V(k) = -2\pi \hbar c \alpha \frac{1}{k(\epsilon + r_0 k)}, \quad (19)$$

with  $\alpha$  the fine-structure constant,  $\epsilon$  the mean dielectric constant of the media surrounding the bilayer, and  $r_0$  as an in-plane screening length [72] related to the polarizability of the material and usually obtained from DFT calculations [73]. The effective screening length can be taken as a first approximation from the dipolar transition amplitudes and is given by [72]

$$r_0 = \frac{\hbar^3 c \alpha}{\pi m_0^2} \int \frac{|\langle c_{\mathbf{k}} | P_{cv\mathbf{k}}^x | v_{\mathbf{k}} \rangle|^2}{E_{cv\mathbf{k}}^3} d^2\mathbf{k}. \quad (20)$$

This effective screening length is very sensitive to the external bias, falling quickly as  $V$  increases, as can be seen in Fig. 3. For the considered bias potential,  $r_0 \approx 103 \text{ \AA}$ . Similarly to previous studies [20], the dielectric constant is set at  $\epsilon = 6.9$  which corresponds to the case of BBG encapsulated in hBN at the zero-frequency limit [74].

We then consider the excitonic wave function to have a well-defined angular momentum  $\ell_n$ , writing it as

$$\psi_{cv\mathbf{k}}^{(n)} = f_{cv\mathbf{k}}^{(n)} e^{i\ell_n\theta_k}. \quad (21)$$

As the band's structure is isotropic, we replace  $E_{cv\mathbf{k}} \rightarrow E_{cvk}$ , allowing us to rewrite the Bethe-Salpeter equation converting the sum into an integral as

Eq. (25) in fact originates from the Rytova-Keldysh potential, as written in Eq. (19), corresponding to the charges being separated in the  $z$  direction. It is, however, simpler to write this factor in the form factor as to explicitly couple only eigenvector components from opposing layers. As required, when the interlayer separation vanishes there will no longer be a vertical separation of the charges and the form factor exactly matches Eq. (23).

Finally, Eq. (22) is solved numerically via the same numerical procedure as described in Sec. II, namely, by considering a tangent grid  $q = \tan(x\frac{\pi}{2})$  with 1500 points  $x \in [0, 1]$ , following the procedure already outlined several times in the literature, namely, in Refs. [20,64–66]. Additionally, due to the introduction of the  $e^{-d|\mathbf{k}-\mathbf{q}|}$  in Eq. (25), the angular integral in Eq. (22) is done numerically in a uniform grid with 1500 points  $\varphi \in [0, 2\pi]$ .

When discussing excitonic states, we will use a similar nomenclature as in the 2D hydrogen atom [75] to distinguish the different angular momentum states (i.e.,  $s$ ,  $p_{\pm}$ ,  $d_{\pm}$  states). In Fig. 4, we plot the binding energy of the first four states of the  $s$ ,  $p_{-}$ , and  $d_{-}$  series. As the bias potential  $V$  increases, the energies of the first  $s$  and  $p_{-}$  states approach each other, eventually crossing in the same way as presented in current *ab initio* computations [21]. In the model considered in this paper, this crossing occurs for a bias potential  $V_{s-p_{-}} \approx 180 \text{ meV}$  and will lead to a swap of the first two peaks of the

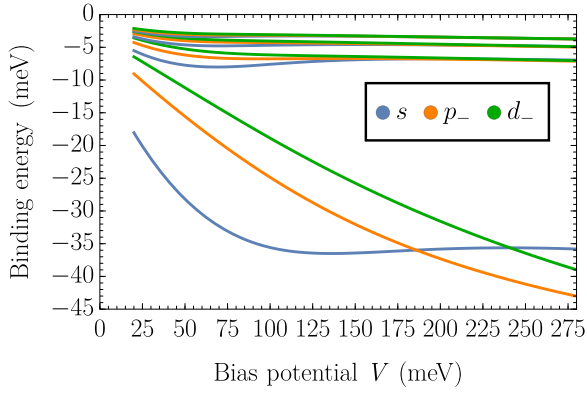


FIG. 4. Evolution of the binding energies of the first four  $s$ ,  $p_-$ , and  $d_-$  series excitons as a function of external bias  $V$ , as obtained from the solution of the BSE as presented in Eqs. (22)–(25).

linear conductivity, as seen in Ref. [21]. The second crossing, involving  $s$  and  $d_-$  states, will occur at  $V_{s-d_-} \approx 245$  meV, and will lead to the dominant resonance for the linear OOP response being at a lower energy than the  $1s$  resonance of the linear IP response.

#### IV. EXCITONIC OPTICAL RESPONSE

Having discussed the method for solving the BSE in a BBG system, we now proceed to the study of the excitonic optical

conductivity, writing the linear conductivity as [53,63]

$$\frac{\sigma_{\alpha\beta}(\omega)}{\sigma_0} = \frac{-i\hbar^2}{2\pi^3 m_0^2} \sum_n \left[ \frac{E_n X_{0n}^\alpha X_{n0}^\beta}{E_n - \hbar\omega} - (\omega \rightarrow -\omega)^* \right], \quad (26)$$

where  $\sigma_0 = \frac{e^2}{4\hbar}$  is the conductivity of monolayer graphene. The excitonic matrix elements are defined as [53,55,63]

$$X_{0n}^\alpha = i \int \psi_{cv\mathbf{k}}^{(n)} \frac{P_{vck}^\alpha}{E_{cv\mathbf{k}}} d^2\mathbf{k}. \quad (27)$$

For the nonlinear conductivity, we define  $\sigma_2 = \frac{e^3 a}{4E_g \hbar}$  and write the SHG ( $\omega_p = \omega_q$ ) nonlinear conductivity [53,63] as

$$\begin{aligned} \frac{\sigma_{\alpha\beta\gamma}^{\text{SHG}}(\omega)}{\sigma_2} = & \frac{-iE_g \hbar^2}{2a\pi^3 m_0^2} \sum_{n,m} \left[ \frac{E_n X_{0n}^\alpha Q_{nm}^\beta X_{m0}^\gamma}{(E_n - 2\hbar\omega)(E_m - \hbar\omega)} \right. \\ & - \frac{E_n X_{n0}^\alpha Q_{nm}^\beta X_{0m}^\gamma}{(E_n + 2\hbar\omega)(E_m + \hbar\omega)} \\ & \left. - \frac{(E_n - E_m) X_{0n}^\alpha Q_{nm}^\beta X_{m0}^\gamma}{(E_n + \hbar\omega)(E_m - \hbar\omega)} \right], \quad (28) \end{aligned}$$

where  $E_g$  is the band gap of the material. As we are only considering effects from the two  $\eta = 1$  bands, we will take the band gap  $E_g$  as  $E_g^{(11)}$ , as discussed earlier. The two-state excitonic matrix elements are defined as [53,55,63]

$$Q_{nm}^\alpha = i \int \psi_{cv\mathbf{k}}^{(n)*} [\psi_{cv\mathbf{k}}^{(m)}]_{:k_\alpha} d^2\mathbf{k}, \quad (29)$$

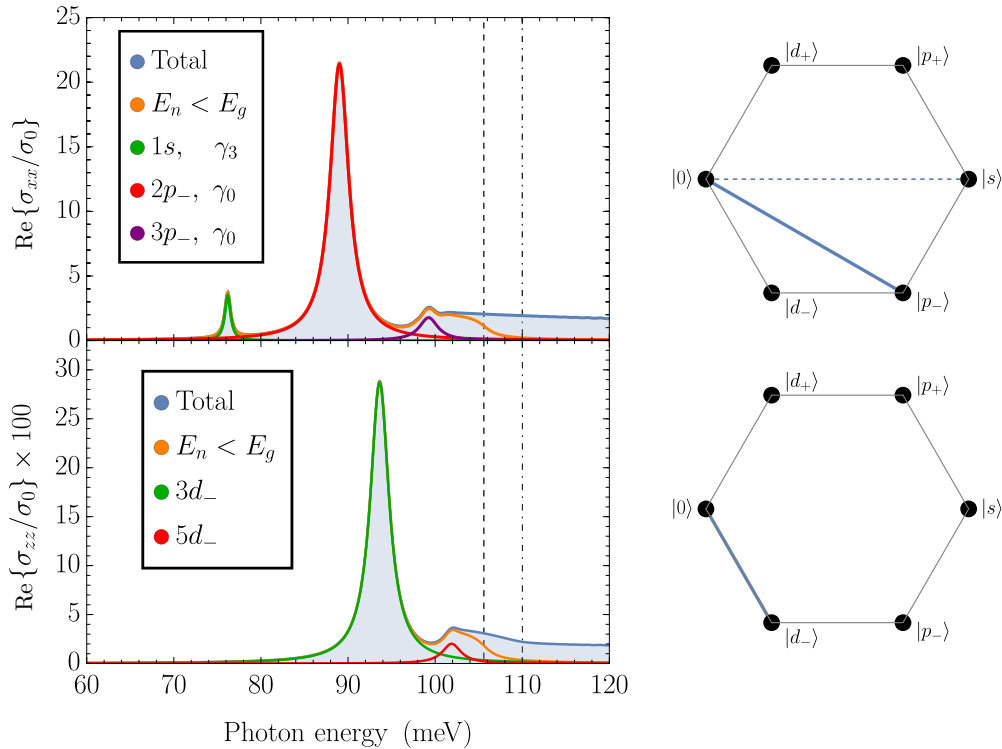


FIG. 5. (Left) Real part of the linear IP (top) and OOP (bottom) optical responses for  $\epsilon_{\text{medium}} = 6.9$ , with  $\hbar\Gamma_{p_-} = \hbar\Gamma_{d_-} = 1.3$  meV and  $\hbar\Gamma_s = 0.4$  meV. Orange curve corresponds to the excitonic bound states, while blue line also includes continuum states. Vertical dashed line represents the band gap  $E_g^{(11)}$  of the system, dotted-dashed line represents  $2V = 110$  meV. In the IP legend,  $\gamma_3$  and  $\gamma_0$  identify which matrix elements allow for the transition in question. (Right) Diagram of dominant excitonic angular momentum selection rules in the  $\tau = 1$  valley for linear IP (top) and OOP (bottom) optical responses. Transitions allowed with (without) skew coupling are shown in dashed (solid) lines.

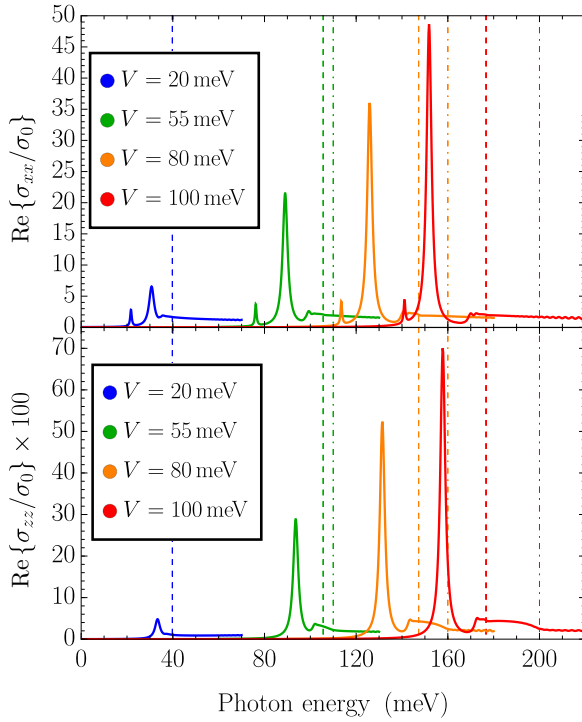


FIG. 6. Real part of the linear IP (top) and OOP (bottom) optical responses for  $\epsilon = 6.9$ , with  $\hbar\Gamma_{p-} = \hbar\Gamma_{d-} = 1.3$  meV and  $\hbar\Gamma_s = 0.4$  meV, for values of the bias potential  $V$  between 20 and 100 meV. Vertical dashed lines represent the band gap  $E_g^{(11)}$  of the system for each value of the bias potential  $V$ , dotted-dashed lines represent the gap at  $k = 0$ , equal to  $2V$ .

where  $[\psi_{cv\mathbf{k}}^{(m)}]_{;k_\alpha}$  is the generalized derivative [54] in the  $\alpha$  direction of the exciton wave function for the state  $m$  given in terms of the Berry connection  $\Omega_{ij\mathbf{k}}^\alpha$ , defined as [63]

$$[\psi_{cv\mathbf{k}}^{(m)}]_{;k_\alpha} = \frac{\partial \psi_{cv\mathbf{k}}^{(m)}}{\partial k_\alpha} - i(\Omega_{cck}^\alpha - \Omega_{v\mathbf{v}\mathbf{k}}^\alpha) \psi_{cv\mathbf{k}}^{(m)}. \quad (30)$$

As the excitonic wave function will be independent of  $k_z$ , the  $\frac{\partial}{\partial k_z} \psi_{cv\mathbf{k}}^{(m)}$  term is dropped, meaning that  $Q_{nm}^z$  reads as [55]

$$Q_{nm}^z = \int \psi_{cv\mathbf{k}}^{(n)*} (\Omega_{cck}^z - \Omega_{v\mathbf{v}\mathbf{k}}^z) \psi_{cv\mathbf{k}}^{(m)} d^2\mathbf{k}. \quad (31)$$

### A. In-plane linear response

Recalling Eq. (27), the excitonic selection rules for IP linear response are obtained directly by considering the angular integral

$$\int_0^{2\pi} e^{i\ell_n\theta} P_{v\mathbf{c}\mathbf{k}}^x d\theta, \quad (32)$$

where  $P_{v\mathbf{c}\mathbf{k}}^x$  is as defined in Eq. (9). Direct inspection of this integral tells us that the terms proportional to  $\gamma_0$  will lead to contributions from states with  $\ell_n = \pm\tau$ , while the presence of skew coupling  $\gamma_3$  allows transitions to states where  $\ell_n = \pm 2\tau$ . This means that the  $X_{0n}^x$  matrix element can be written, in a

somewhat abusive but concise form, as

$$X_{0n}^x = X_{\ell_n+\tau=0}^x + X_{\ell_n-\tau=0}^x - i\frac{\gamma_3}{\gamma_0} [X_{\ell_n+2\tau=0}^x - X_{\ell_n-2\tau=0}^x], \quad (33)$$

where the new indices restrict each term to the Kronecker  $\delta$ 's resulting from the different angular integrals. Taking  $|X_{0n}^x|^2$  as in Eq. (26), the presence of the various Kronecker  $\delta$ 's originating from each of the angular integrals means that non-vanishing contributions from  $\gamma_3$  to the linear response must be proportional to  $|\gamma_3|^2$ . Therefore, the inclusion of an  $i$  factor in the Hamiltonian will not alter the results when compared to previous studies [20]. It will, however, affect the nonlinear response as it will be linear in  $\gamma_3$  (in this simple approximation) and, therefore, the  $i$  factor proves to be important.

Following from the results of Ref. [18], we will assume the broadening to be dependent on the excitonic state  $n$ . Specifically, we set the broadening as dependent on the angular momentum series, given by  $\hbar\Gamma_{p-} = 1.3$  meV and  $\hbar\Gamma_s = 0.4$  meV. With the broadening set, we plot the IP linear response for  $V = 55$  meV in the top panel of Fig. 5. Varying the bias potential  $V$ , we can observe the tunability of the IP linear response in the top panel of Fig. 6. Similarly to what was observed in Refs. [20,21], the dominant peak for the IP linear response quickly increases as the bias potential increases. Additionally, the location of the peak corresponding to the  $1s$  resonance approaches that of the dominant  $2p_-$  resonance, as indicated by the evolution of the binding energies in Fig. 4.

### B. In-plane nonlinear response

Now for the nonlinear optical response, we recall Eqs. (29) and (30) and write the integrand present in the two-state momentum matrix element as

$$\psi_{cv\mathbf{k}}^{(n)*} \left[ \frac{\partial \psi_{cv\mathbf{k}}^{(m)}}{\partial k_x} - i(\Omega_{cck}^x - \Omega_{v\mathbf{v}\mathbf{k}}^x) \psi_{cv\mathbf{k}}^{(m)} \right]. \quad (34)$$

Focusing on the angular integration of this expression, and recalling the definition of the Berry connection present in Eq. (12), one obtains that only transitions with  $\ell_m - \ell_n = \pm 1$  are allowed. In a similar notation to Eq. (33), this means that the Berry connection up to zeroth order in  $\frac{\gamma_3}{\gamma_0}$  can be written as

$$Q_{nm}^x = Q_{|\ell_m - \ell_n| = 1}^x. \quad (35)$$

Multiplication of the angular momentum Kronecker  $\delta$ 's from Eqs. (33)–(35) leads to four nonzero matrix elements which will be linear in  $\frac{\gamma_3}{\gamma_0}$ . We denote these nonzero matrix elements by the oscillator strength defined, for compactness, as

$$\sigma_{\ell_n; \ell_m} \equiv X_{\ell_n}^x Q_{\ell_n, \ell_m}^x X_{\ell_m}^x. \quad (36)$$

Explicitly, the transitions allowed by Eqs. (32)–(34) will be

$$\begin{array}{cc} \sigma_{s;p-}, & \sigma_{p-;s}, \\ \sigma_{f-;g-}, & \sigma_{g-;f-}, \end{array} \quad (37)$$

where the left column corresponds to those where  $\ell_m - \ell_n = -1$  and the right column to those where  $\ell_m - \ell_n = 1$ .

Careful inspection of the matrix elements tells us that  $\sigma_{s;p-}$  and  $\sigma_{p-;s}$  will be the dominant contributions to the SHG

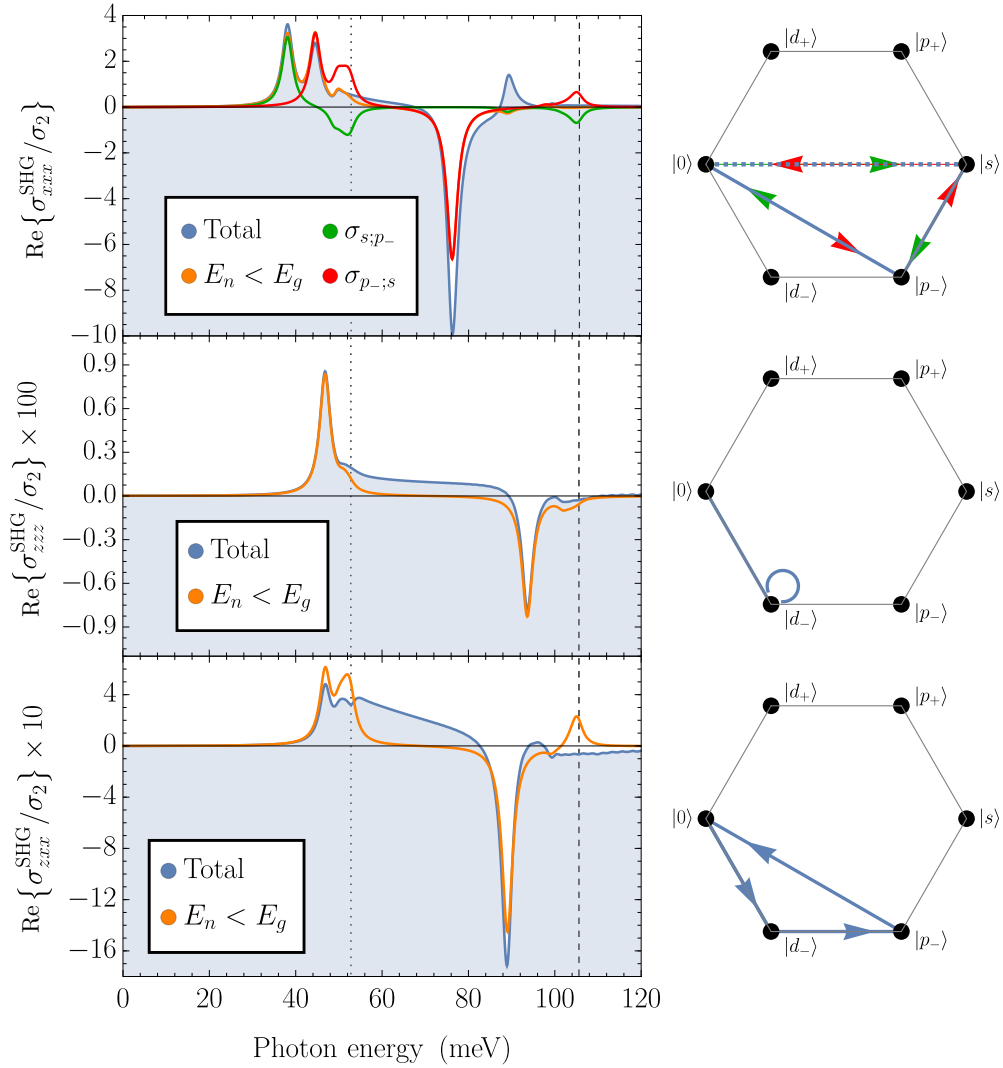


FIG. 7. (Left) Real part of the SHG optical response of BBG with diagonal IP (top), diagonal OOP (middle), and nondiagonal OOP (bottom) conductivity for  $\epsilon_{\text{medium}} = 6.9$  and  $\hbar\Gamma = 1.5$  meV. Orange curve corresponds to only excitonic bound states, while blue line also includes continuum states. Vertical (dotted) dashed black lines represent (half) the band gap  $E_g^{(11)}$  of the system. (Right) Diagram of dominant excitonic angular momentum selection rules in the  $\tau = 1$  valley for each component. Transitions allowed with (without) skew coupling are shown in dashed (solid) lines. Arrow direction and color represent the specific resonance when multiple contributions are present.

nonlinear response up to linear order in  $\frac{\gamma_2}{\gamma_0}$ . The real part of the SHG nonlinear response is then plotted in the top panel of Fig. 7. Similarly to previous results [55], we see that the dominant contribution will originate from the excitonic states with the smallest angular momentum.

### C. Out-of-plane linear response

Recalling Eq. (27), the dipole transition amplitude for the excitonic state  $n$  with angular momentum quantum number  $\ell_n$  reads as

$$X_{0n}^z = \int_0^\infty \frac{f_{cvk}^{(n)}}{E_{cvk}} k dk \int_0^{2\pi} e^{i\ell_n\theta} P_{vck}^z d\theta \quad (38)$$

which immediately leads to the optical selection rule  $\ell_n = 0$  for the linear response when one recalls the definition of  $P_{vck}^z$  from Eq. (15). Inspecting this equation also tells us

that the OOP linear optical response will have a quadratic dependence on the interlayer spacing, originating directly from  $|\int_0^{2\pi} e^{i\ell_n\theta} P_{vck}^z d\theta|^2$ . Additionally, a more complex dependence on  $d$  will be implicitly present in the excitonic wave function  $f_{cvk}^{(n)}$  due to the exponential  $e^{-d|\mathbf{k}-\mathbf{q}|}$  in the form factor present in Eq. (25).

The real part of the OOP linear excitonic optical response is plotted in the bottom panel of Fig. 5, together with the diagram of the allowed transitions in the  $\tau = 1$  valley. Although it is not labeled in the figure due to its much weaker amplitude, the  $4d_-$  transition is still allowed. Contrary to what was computed for the OOP linear response of a buckled monolayer [55], we observe that the conductivity quickly stabilizes to a constant value for  $\hbar\omega > E_g^{(11)}$ , while in a buckled monolayer an apparently linear growth with  $\hbar\omega$  was observed in the same regime. The observed behavior also matches with the results for the free-carrier conductivity, present in the bottom panel of Fig. 2,



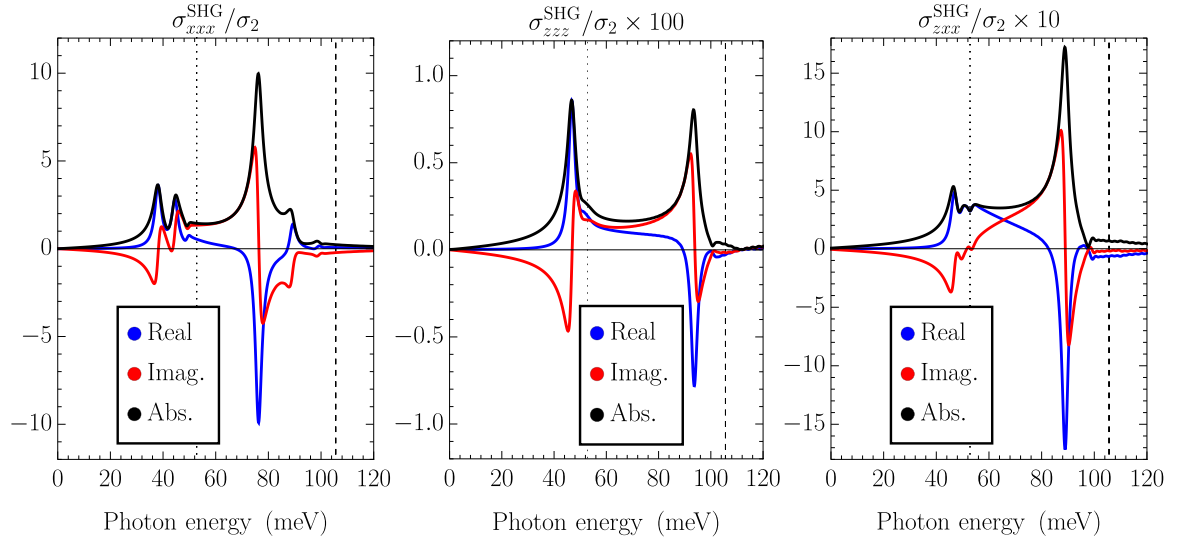


FIG. 8. Real (blue) and imaginary (red) parts, as well as absolute value (black) of the  $xxx$  (left),  $zzz$  (middle), and  $zxx$  (right) tensor elements of the excitonic SHG nonlinear conductivity for  $\epsilon_{\text{medium}} = 6.9$  and  $\hbar\Gamma = 1.5$  meV. Vertical (dotted) dashed black lines represent (half) the band gap  $E_g^{(11)}$  of the system.

in the region where the two-band approximation is valid. Additionally, in the bottom panel of Fig. 6, we present the OOP optical response for various values of the bias potential  $V$  between 20 and 100 meV. In this figure, we can see the much larger effect of the bias potential on the OOP optical response in comparison to the IP response. This is most noticeable between  $V = 20$  and 55 meV, where the maximum of the linear response for the IP and OOP linear response increases by factors of approximately  $3\times$  and  $5\times$ , respectively.

### D. Out-of-plane nonlinear response

Focusing now on the OOP nonlinear regime, we recall the expression for  $Q_{nm}^z$  from Eq. (31) as

$$Q_{nm}^z = \int \psi_{cv\mathbf{k}}^{(n)*} (\Omega_{cck}^z - \Omega_{v\mathbf{k}}^z) \psi_{cv\mathbf{k}}^{(m)} d^2\mathbf{k}. \quad (39)$$

With this expression in mind, careful analysis of Eq. (16) leads immediately to the selection rules

$$\ell_n = \ell_m. \quad (40)$$

This selection rule is rather unrestrictive, meaning that it will be  $X_{0n}^z$  which will determine the allowed transitions.

Focusing first on the diagonal  $\sigma_{zzz}$  response, the selection rules follow immediately from analysis of  $X_{0n}^z$  and  $Q_{nm}^z$  as

$$\ell_n = \ell_m = 0. \quad (41)$$

Recalling the pseudospin factor, this means that the transitions present will be associated with  $d_-$  series states. Knowing the selection rules, we can compute the SHG conductivity, plotted in the middle panel of Fig. 7. The matrix elements  $X_{0n}^z$  (around  $\frac{1}{5}$  the magnitude of  $X_{0n}^x$ ) and  $Q_{nm}^z$  (around  $\frac{1}{4}$  the magnitude of the analogous matrix element in  $Q_{nm}^x$ ) are significantly smaller than those present in  $\sigma_{xxx}^{\text{SHG}}$ . This, in conjunction with the cubic dependence [55] on the ratio  $d/a \approx 0.7$ , means that the peak amplitude of  $\sigma_{zzz}^{\text{SHG}}$  is close to 800 times smaller than that of  $\sigma_{xxx}^{\text{SHG}}$ . A big difference can also be observed in the qualitative

behavior of  $\sigma_{zzz}^{\text{SHG}}$  versus its analogous counterpart in a buckled monolayer [55]: while in the buckled monolayer the  $\sigma_{zzz}^{\text{SHG}}$  response above the band gap remains close to its maximum, in BBG we observe that it quickly tends to a much smaller value, similarly to what is observed in the  $\sigma_{xxx}^{\text{SHG}}$  response.

Second, we focus our attention on the off-diagonal  $\sigma_{zxx}$  response. While the presence of  $X_{0n}^z$  means immediately that  $\ell_n = 0$ , we must now carefully analyze Eqs. (9)–(32), as well as Eqs. (12)–(34). From  $Q_{nm}^x$ , we immediately get that

$$|\ell_m - \ell_n| = 1 \Rightarrow \ell_m = \pm 1,$$

both allowed by the selection rules for  $X_{m0}^x$ . Hence, we are restricted to states

$$\ell_n = 0, \quad \ell_m = \pm 1.$$

Again recalling the pseudospin factor, we can immediately associate the selection rules with transitions between  $d_-$  states and both  $p_-$  and  $f_-$  states. Careful inspection of the oscillator strength for the two distinct selection rules reveals that, as one would intuitively expect from the lower angular momentum, resonances associated with the matrix elements  $\sigma_{d_-;p_-}$  dominate. The off-diagonal  $\sigma_{zxx}^{\text{SHG}}$  SHG response is then plotted in the bottom panel of Fig. 7.

For better readability and to facilitate comparisons with experimental results, the real and imaginary parts of the three tensor elements presented in Fig. 7 are presented separately in Fig. 8, together with the absolute value of each tensor element for a bias voltage  $V = 55$  meV. This specific bias voltage is chosen so that the band gap  $E_g^{(11)}$  is still much smaller than the excitonic resonances associated with the second band gap, namely, close to  $2\hbar\omega = E_g^{(12)}$ , meaning that the effects of these missing resonances on the imaginary part will be minimized. It is important to note that, while the two-band BSE results for the imaginary part will drift away from the four-band results at higher energies, as discussed previously in Sec. II, these will be qualitatively correct in regards to the

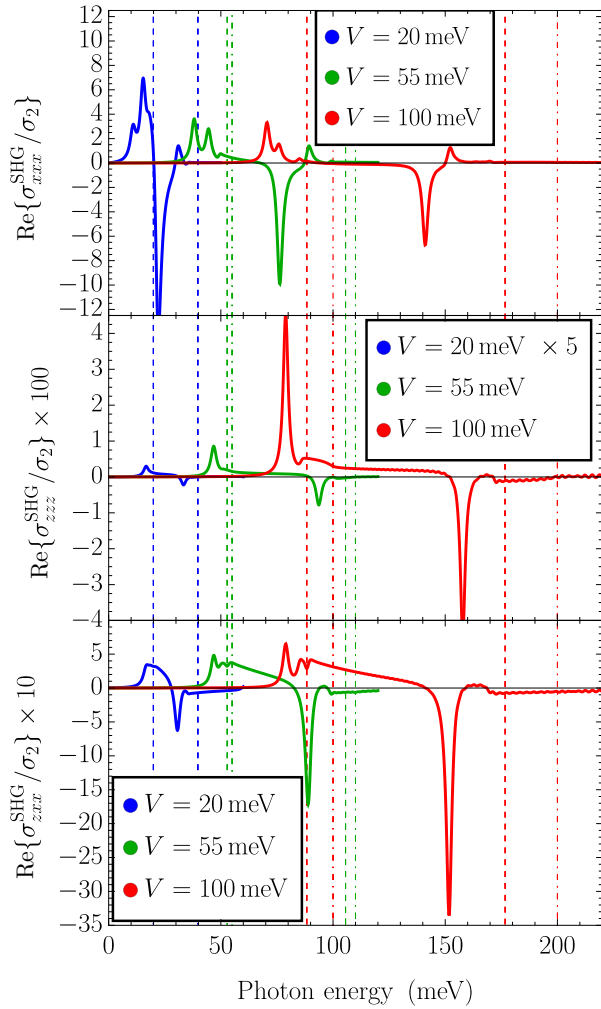


FIG. 9. Real part of the SHG IP (top), diagonal OOP (middle), and nondiagonal OOP (bottom) optical responses for  $\epsilon = 6.9$ , with broadening  $\hbar\Gamma = 1.5$  meV, for values of the bias potential  $V$  between 20 and 100 meV. Vertical dashed lines represent the band gap  $E_g^{(11)}$  of the system for each value of the bias potential  $V$ , dotted-dashed lines represent the gap at  $k = 0$ , equal to  $2V$ . Leftmost vertical lines correspond to response at  $2\hbar\omega$ , rightmost vertical lines correspond to response at  $\hbar\omega$ .

location of the resonances for the frequency range considered. The imaginary part and absolute value can, therefore, prove themselves useful for comparison against experimental results [44–47].

Finally, in Fig. 9, we present the SHG IP (top), diagonal OOP (middle), and nondiagonal OOP (bottom) optical responses for three different values of the bias potential  $V$ . In this figure, we keep a constant broadening  $\hbar\Gamma = 1.5$  meV as to more easily observe the effects of tuning the bias potential. For the lowest value of the bias potential,  $V = 20$  meV, the lowest band gap  $E_g^{(11)} = 39.8$  meV is very close to  $2V = 40$  meV, we only keep the vertical lines associated with  $E_g^{(11)}$  and  $E_g^{(11)}/2$  for improved readability. Starting with the IP response  $\sigma_{xxx}^{\text{SHG}}$ , we can observe that, at  $V = 20$  meV, the proximity between the multiple resonances leads to a sharp increase in intensity when compared with the response at  $V = 55$  and 100 meV. Additionally, the much larger separation between the

$2\hbar\omega = E_n$  and the  $\hbar\omega = E_n$  regions of the plot (i.e.,  $E_g^{(11)}/2 \leq \hbar\omega \leq E_g^{(11)}$ ) and the specific form of the IP generalized derivative as defined in Eq. (30) leads to the slight decrease of the IP  $\sigma_{xxx}^{\text{SHG}}$  with increasing bias potential. For the diagonal OOP response  $\sigma_{zzz}^{\text{SHG}}$ , we observe that the magnitude of the excitonic response quickly grows with the bias potential  $V$ . This follows what is expected, as it is the OOP anisotropy due to the bias potential that leads to a nonzero OOP response. Lastly, the nondiagonal OOP response  $\sigma_{zxx}^{\text{SHG}}$  also presents an increasing magnitude with the bias potential  $V$ , as expected from the growing OOP anisotropy. The nature of the nondiagonal response, with its mixing of IP and OOP components, means that the response at low bias potential (see  $V = 20$  meV regime) does not vanish as quickly as the  $\sigma_{zzz}^{\text{SHG}}$  component. Additionally, direct comparison between top and bottom panels of Fig. 9 shows that, as bias potential increases, the magnitude of the nondiagonal OOP response approaches that of the IP response, with the maximum of  $\sigma_{zxx}^{\text{SHG}}$  approximately  $\frac{1}{2}$  that of  $\sigma_{xxx}^{\text{SHG}}$  for  $V = 100$  meV.

## V. SUMMARY

In this paper, we studied the excitonic linear and nonlinear optical responses of Bernal-stacked BBG as a function of the gate voltage, both for in-plane (IP) and out-of-plane (OOP) directions. Starting with the electronic structure of BBG, we consider the influence of gate voltage on the band structure of the system. Taking into account the three distinct band gaps present, we introduce a two-band approximation that greatly simplifies the numerical complexity of the problem. Outlining the generic form of the momentum matrix elements and Berry connections, we compute the linear IP and OOP free-carrier optical responses for both the two-band approximation and the full four-band Hamiltonian. The large separation of the higher-energy bands (for  $V = 55$  meV, the lowest band gap is  $E_g^{(11)} = 106$  meV while the second lowest is  $E_g^{(12)} = 436$  meV) means that, for frequency below  $E_g^{(12)}$ , the real part of the optical response is very accurately described by the two-band approximation.

Under this two-band approximation, we then computed the excitonic states in the system by numerical diagonalization of the Bethe-Salpeter equation, studying the evolution of the excitonic binding energies as a function of external bias potential.

Knowing the excitonic states, together with the momentum matrix elements and Berry connections, allowed us to then explicitly discuss the excitonic selection rules of the system for both the IP and OOP excitonic responses. The inclusion of skew coupling in the momentum matrix elements proves fundamental in obtaining a nonzero IP nonlinear response, as well as introducing  $s$ -series resonances in the IP linear response. For the OOP linear response the OOP anisotropy proves to be sufficient for obtaining a nonzero linear and nonlinear response.

Both linear and SHG nonlinear responses are very sensitive to the tuning of the bias voltage, where the effects of tuning the bias voltage on the linear IP response have been discussed previously in the literature [20,21]. First, tuning the bias potential will directly affect the band gap of the system, leading

to a tuning of the excitonic binding energies and, therefore, the location of the resonant peaks in the optical response, as well as on the interband momentum matrix elements. Additionally, as the OOP anisotropy is controlled by the bias potential, its effects on the OOP response are not as simple as those on the IP response.

### ACKNOWLEDGMENTS

M.F.C.M.Q. acknowledges the International Iberian Nanotechnology Laboratory (INL) and the Portuguese

Foundation for Science and Technology (FCT) for the Quantum Portugal Initiative (QPI) Grant No. SFRH/BD/151114/2021. N.M.R.P. acknowledges support by the Portuguese Foundation for Science and Technology (FCT) in the framework of the Strategic Funding UIDB/04650/2020, COMPETE 2020, PORTUGAL 2020, FEDER, and FCT through projects PTDC/FIS-MAC/2045/2021 and EXPL/FIS-MAC/0953/2021. N.M.R.P. also acknowledges the Independent Research Fund Denmark (Grant No. 2032-00045B) and the Danish National Research Foundation (Project No. D NRF165).

- 
- [1] K. S. Novoselov, A. K. Geim, S. V. Morozov, D. Jiang, Y. Zhang, S. V. Dubonos, I. V. Grigorieva, and A. A. Firsov, Electric field effect in atomically thin carbon films, *Science* **306**, 666 (2004).
- [2] A. Taghizadeh, K. S. Thygesen, and T. G. Pedersen, Two-dimensional materials with giant optical nonlinearities near the theoretical upper limit, *ACS Nano* **15**, 7155 (2021).
- [3] J. D. Caldwell, I. Aharonovich, G. Cassabois, J. H. Edgar, B. Gil, and D. N. Basov, Photonics with hexagonal boron nitride, *Nat. Rev. Mater.* **4**, 552 (2019).
- [4] G. Wang, A. Chernikov, M. M. Glazov, T. F. Heinz, X. Marie, T. Amand, and B. Urbaszek, Colloquium: Excitons in atomically thin transition metal dichalcogenides, *Rev. Mod. Phys.* **90**, 021001 (2018).
- [5] H. Şahin, S. Cahangirov, M. Topsakal, E. Bekaroglu, E. Akturk, R. T. Senger, and S. Ciraci, Monolayer honeycomb structures of group-IV elements and III-V binary compounds: First-principles calculations, *Phys. Rev. B* **80**, 155453 (2009).
- [6] H. K. Avetissian and G. F. Mkrtchian, Higher harmonic generation by massive carriers in buckled two-dimensional hexagonal nanostructures, *Phys. Rev. B* **99**, 085432 (2019).
- [7] M.-Q. Le, H.-T. Nguyen, and T.-L. Bui, Fracture of 28 buckled two-dimensional hexagonal sheets, *Mech. Adv. Mater. Struct.* **29**, 4993 (2022).
- [8] R. Y. Kezerashvili and A. Spiridonova, Effects of parallel electric and magnetic fields on Rydberg excitons in buckled two-dimensional materials, *Phys. Rev. B* **103**, 165410 (2021).
- [9] A.-Y. Lu, H. Zhu, J. Xiao, C.-P. Chuu, Y. Han, M.-H. Chiu, C.-C. Cheng, C.-W. Yang, K.-H. Wei, Y. Yang, Y. Wang, D. Sokaras, D. Nordlund, P. Yang, D. A. Muller, M.-Y. Chou, X. Zhang, and L.-J. Li, Janus monolayers of transition metal dichalcogenides, *Nat. Nanotechnol.* **12**, 744 (2017).
- [10] J. Zhang, S. Jia, I. Kholmanov, L. Dong, D. Er, W. Chen, H. Guo, Z. Jin, V. B. Shenoy, L. Shi, and J. Lou, Janus monolayer transition-metal dichalcogenides, *ACS Nano* **11**, 8192 (2017).
- [11] T. Zheng, Y.-C. Lin, Y. Yu, P. Valencia-Acuna, A. A. Puzos, R. Torsi, C. Liu, I. N. Ivanov, G. Duscher, D. B. Geohegan, Z. Ni, K. Xiao, and H. Zhao, Excitonic dynamics in janus MoSSe and WSSe monolayers, *Nano Lett.* **21**, 931 (2021).
- [12] O. Dogadov, C. Trovatello, B. Yao, G. Soavi, and G. Cerullo, Parametric nonlinear optics with layered materials and related heterostructures, *Laser Photon. Rev.* **16**, 2100726 (2022).
- [13] J. Shi, H. Xu, C. Heide, C. HuangFu, C. Xia, F. de Quesada, H. Shen, T. Zhang, L. Yu, A. Johnson, F. Liu, E. Shi, L. Jiao, T. Heinz, S. Ghimire, J. Li, J. Kong, Y. Guo, and A. M. Lindenberg, Giant room-temperature nonlinearities in a monolayer janus topological semiconductor, *Nat. Commun.* **14**, 4953 (2023).
- [14] C.-H. Park and S. G. Louie, Tunable excitons in biased bilayer graphene, *Nano Lett.* **10**, 426 (2010).
- [15] Y. Gong, J. Lin, X. Wang, G. Shi, S. Lei, Z. Lin, X. Zou, G. Ye, R. Vajtai, B. I. Yakobson, H. Terrones, M. Terrones, B.-K. Tay, J. Lou, S. T. Pantelides, Z. Liu, W. Zhou, and P. M. Ajayan, Vertical and in-plane heterostructures from WS<sub>2</sub>/MoS<sub>2</sub> monolayers, *Nat. Mater.* **13**, 1135 (2014).
- [16] P. Rivera, K. L. Seyler, H. Yu, J. R. Schaibley, J. Yan, D. G. Mandrus, W. Yao, and X. Xu, Valley-polarized exciton dynamics in a 2D semiconductor heterostructure, *Science* **351**, 688 (2016).
- [17] S. J. Brun and T. G. Pedersen, Intense and tunable second-harmonic generation in biased bilayer graphene, *Phys. Rev. B* **91**, 205405 (2015).
- [18] L. Ju, L. Wang, T. Cao, T. Taniguchi, K. Watanabe, S. G. Louie, F. Rana, J. Park, J. Hone, F. Wang, and P. L. McEuen, Tunable excitons in bilayer graphene, *Science* **358**, 907 (2017).
- [19] A. A. Avetisyan, A. P. Djotyan, and K. Mouloupoulos, Tunable excitons in bilayer graphene with opened energy gap, *Phys. At. Nucl.* **81**, 799 (2018).
- [20] J. C. G. Henriques, I. Epstein, and N. M. R. Peres, Absorption and optical selection rules of tunable excitons in biased bilayer graphene, *Phys. Rev. B* **105**, 045411 (2022).
- [21] M. O. Sauer and T. G. Pedersen, Exciton absorption, band structure, and optical emission in biased bilayer graphene, *Phys. Rev. B* **105**, 115416 (2022).
- [22] H. D. Scammell and O. P. Sushkov, Dynamical screening and excitonic bound states in biased bilayer graphene, *Phys. Rev. B* **107**, 085104 (2023).
- [23] T. Ando and M. Koshino, Optical absorption by interlayer density excitations in bilayer graphene, *J. Phys. Soc. Jpn.* **78**, 104716 (2009).
- [24] M.-E. Kleemann, R. Chikkaraddy, E. M. Alexeev, D. Kos, C. Carnegie, W. Deacon, A. C. de Pury, C. Große, B. de Nijs, J. Mertens, A. I. Tartakovskii, and J. J. Baumberg, Strong-coupling of WSe<sub>2</sub> in ultra-compact plasmonic nanocavities at room temperature, *Nat. Commun.* **8**, 1296 (2017).
- [25] M. Stührenberg, B. Munkhbat, D. G. Baranov, J. Cuadra, A. B. Yankovich, T. J. Antosiewicz, E. Olsson, and T. Shegai, Strong light-matter coupling between plasmons in individual gold bi-pyramids and excitons in mono- and multilayer WSe<sub>2</sub>, *Nano Lett.* **18**, 5938 (2018).

- [26] A. Dasgupta, J. Gao, and X. Yang, Atomically thin nonlinear transition metal dichalcogenide holograms, *Nano Lett.* **19**, 6511 (2019).
- [27] G. Soavi, G. Wang, H. Rostami, D. G. Purdie, D. De Fazio, T. Ma, B. Luo, J. Wang, A. K. Ott, D. Yoon, S. A. Bourelle, J. E. Muench, I. Goykhman, S. Dal Conte, M. Celebrano, A. Tomadin, M. Polini, G. Cerullo, and A. C. Ferrari, Broadband, electrically tunable third-harmonic generation in graphene, *Nat. Nanotechnol.* **13**, 583 (2018).
- [28] S. Klimmer, O. Ghaebi, Z. Gan, A. George, A. Turchanin, G. Cerullo, and G. Soavi, All-optical polarization and amplitude modulation of second-harmonic generation in atomically thin semiconductors, *Nat. Photon.* **15**, 837 (2021).
- [29] Y. Zhang, Y. Wang, Y. Dai, X. Bai, X. Hu, L. Du, H. Hu, X. Yang, D. Li, Q. Dai, T. Hasan, and Z. Sun, Chirality logic gates, *Sci. Adv.* **8**, eabq8246 (2022).
- [30] Y. Li, N. An, Z. Lu, Y. Wang, B. Chang, T. Tan, X. Guo, X. Xu, J. He, H. Xia, Z. Wu, Y. Su, Y. Liu, Y. Rao, G. Soavi, and B. Yao, Nonlinear co-generation of graphene plasmons for optoelectronic logic operations, *Nat. Commun.* **13**, 3138 (2022).
- [31] Z. Zheng, K. Chang, and J. L. Cheng, Gate voltage induced injection and shift currents in aa- and ab-stacked bilayer graphene, *Phys. Rev. B* **108**, 235401 (2023).
- [32] T. Ohta, A. Bostwick, T. Seyller, K. Horn, and E. Rotenberg, Controlling the electronic structure of bilayer graphene, *Science* **313**, 951 (2006).
- [33] F. Guinea, A. H. Castro Neto, and N. M. R. Peres, Electronic states and Landau levels in graphene stacks, *Phys. Rev. B* **73**, 245426 (2006).
- [34] T. Stauber, N. M. R. Peres, and A. K. Geim, Optical conductivity of graphene in the visible region of the spectrum, *Phys. Rev. B* **78**, 085432 (2008).
- [35] A. V. Rozhkov, A. O. Sboychakov, A. L. Rakhmanov, and F. Nori, Electronic properties of graphene-based bilayer systems, *Phys. Rep.* **648**, 1 (2016).
- [36] C. Ortix, Nonlinear hall effect with time-reversal symmetry: Theory and material realizations, *Adv. Quantum Technol.* **4**, 2100056 (2021).
- [37] E. V. Castro, K. S. Novoselov, S. V. Morozov, N. M. R. Peres, J. M. B. L. dos Santos, J. Nilsson, F. Guinea, A. K. Geim, and A. H. C. Neto, Biased bilayer graphene: Semiconductor with a gap tunable by the electric field effect, *Phys. Rev. Lett.* **99**, 216802 (2007).
- [38] J. M. B. L. dos Santos, N. M. R. Peres, and A. H. C. Neto, Graphene bilayer with a twist: Electronic structure, *Phys. Rev. Lett.* **99**, 256802 (2007).
- [39] Y. Cao, V. Fatemi, S. Fang, K. Watanabe, T. Taniguchi, E. Kaxiras, and P. Jarillo-Herrero, Unconventional superconductivity in magic-angle graphene superlattices, *Nature (London)* **556**, 43 (2018).
- [40] M. M. Quintela, J. Guerra, and S. João, Electronic properties of twisted bilayer graphene in the presence of a magnetic field, *EPJ Web Conf.* **233**, 03004 (2020).
- [41] E. Y. Andrei and A. H. MacDonald, Graphene bilayers with a twist, *Nat. Mater.* **19**, 1265 (2020).
- [42] L. Di M. Villari and A. Principi, Optotwistronics of bilayer graphene, *Phys. Rev. B* **106**, 035401 (2022).
- [43] H. Yu, X. Cui, X. Xu, and W. Yao, Valley excitons in two-dimensional semiconductors, *Nat. Sci. Rev.* **2**, 57 (2015).
- [44] J. Chen, S. Machida, and Y. Yamamoto, Simultaneous measurement of amplitude and phase in surface second-harmonic generation, *Opt. Lett.* **23**, 676 (1998).
- [45] S. K. Andersson, M. C. Schanne-Klein, and F. Hache, Symmetry and phase determination of second-harmonic reflection from calcite surfaces, *Phys. Rev. B* **59**, 3210 (1999).
- [46] S. Yazdanfar, L. H. Laiho, and P. T. C. So, Interferometric second harmonic generation microscopy, *Opt. Express* **12**, 2739 (2004).
- [47] K. C. Jena, P. A. Covert, and D. K. Hore, Phase measurement in nondegenerate three-wave mixing spectroscopy, *J. Chem. Phys.* **134**, 044712 (2011).
- [48] E. McCann and M. Koshino, The electronic properties of bilayer graphene, *Rep. Prog. Phys.* **76**, 056503 (2013).
- [49] S. Di Sabatino, J. A. Berger, and P. Romaniello, Optical spectra of 2D monolayers from time-dependent density functional theory, *Faraday Discuss.* **224**, 467 (2020).
- [50] X. Zhang, W.-Y. Shan, and D. Xiao, Optical selection rule of excitons in gapped chiral fermion systems, *Phys. Rev. Lett.* **120**, 077401 (2018).
- [51] T. Cao, M. Wu, and S. G. Louie, Unifying optical selection rules for excitons in two dimensions: Band topology and winding numbers, *Phys. Rev. Lett.* **120**, 087402 (2018).
- [52] J. C. G. Henriques, B. Amorim, R. M. Ribeiro, and N. M. R. Peres, Excitonic response of AA' and AB stacked hBN bilayers, *Phys. Rev. B* **105**, 115421 (2022).
- [53] A. Taghizadeh and T. G. Pedersen, Nonlinear optical selection rules of excitons in monolayer transition metal dichalcogenides, *Phys. Rev. B* **99**, 235433 (2019).
- [54] C. Aversa and J. E. Sipe, Nonlinear optical susceptibilities of semiconductors: Results with a length-gauge analysis, *Phys. Rev. B* **52**, 14636 (1995).
- [55] M. F. C. M. Quintela and T. G. Pedersen, Anisotropic linear and nonlinear excitonic optical properties of buckled monolayer semiconductors, *Phys. Rev. B* **107**, 235416 (2023).
- [56] K. Yoshizawa, T. Yumura, T. Yamabe, and S. Bandow, The role of orbital interactions in determining the interlayer spacing in graphite slabs, *J. Am. Chem. Soc.* **122**, 11871 (2000).
- [57] M. S. Alam, J. Lin, and M. Saito, First-principles calculation of the interlayer distance of the two-layer graphene, *Jpn. J. Appl. Phys.* **50**, 080213 (2011).
- [58] B. Butz, C. Dolle, F. Niekkel, K. Weber, D. Waldmann, H. B. Weber, B. Meyer, and E. Spiecker, Dislocations in bilayer graphene, *Nature (London)* **505**, 533 (2014).
- [59] Y. Fukaya, Y. Zhao, H.-W. Kim, J. R. Ahn, H. Fukidome, and I. Matsuda, Atomic arrangements of quasicrystal bilayer graphene: Interlayer distance expansion, *Phys. Rev. B* **104**, L180202 (2021).
- [60] V. N. Genkin and P. M. Mednis, Contribution to the theory of nonlinear effects in crystals with account taken of partially filled bands, *Sov. Phys.-JETP* **27**, 609 (1968).
- [61] B. Kirtman, F. L. Gu, and D. M. Bishop, Extension of the Genkin and Mednis treatment for dynamic polarizabilities and hyperpolarizabilities of infinite periodic systems. I. Coupled perturbed Hartree-Fock theory, *J. Chem. Phys.* **113**, 1294 (2000).
- [62] V. A. Margulis, E. E. Muryumin, and E. A. Gaiduk, Optical second-harmonic generation from two-dimensional hexagonal

- crystals with broken space inversion symmetry, *J. Phys.: Condens. Matter* **25**, 195302 (2013).
- [63] T. G. Pedersen, Intraband effects in excitonic second-harmonic generation, *Phys. Rev. B* **92**, 235432 (2015).
- [64] C. Y.-P. Chao and S. L. Chuang, Analytical and numerical solutions for a two-dimensional exciton in momentum space, *Phys. Rev. B* **43**, 6530 (1991).
- [65] D. G. W. Parfitt and M. E. Portnoi, The two-dimensional hydrogen atom revisited, *J. Math. Phys.* **43**, 4681 (2002).
- [66] M. F. C. M. Quintela, J. C. G. Henriques, L. G. M. Tenório, and N. M. R. Peres, Theoretical methods for excitonic physics in 2D materials, *Phys. Status Solidi B* **259**, 2200097 (2022).
- [67] M. F. C. M. Quintela and N. M. R. Peres, Tunable excitons in rhombohedral trilayer graphene, *Phys. Rev. B* **105**, 205417 (2022).
- [68] G. F. Glinskii and Z. Koinov, Functional formulation of microscopic theory of exciton polaritons, *Theor. Math. Phys.* **70**, 252 (1987).
- [69] S. K. Radha, W. R. L. Lambrecht, B. Cunningham, M. Grüning, D. Pashov, and M. van Schilfgaarde, Optical response and band structure of LiCoO<sub>2</sub> including electron-hole interaction effects, *Phys. Rev. B* **104**, 115120 (2021).
- [70] S. N. Rytova, The screened potential of a point charge in a thin film, *Mosc. Un. Phys. Bul.* **3**, 30 (1967).
- [71] L. V. Keldysh, Coulomb interaction in thin semiconductor and semimetal films, *Sov. J. Exp. Theor. Phys. Lett.* **29**, 658 (1979).
- [72] P. Li and I. Appelbaum, Excitons without effective mass: Biased bilayer graphene, *Phys. Rev. B* **99**, 035429 (2019).
- [73] T. Tian, D. Scullion, D. Hughes, L. H. Li, C.-J. Shih, J. Coleman, M. Chhowalla, and E. J. G. Santos, Electronic polarizability as the fundamental variable in the dielectric properties of two-dimensional materials, *Nano Lett.* **20**, 841 (2020).
- [74] A. Laturia, M. L. Van de Put, and W. G. Vandenberghe, Dielectric properties of hexagonal boron nitride and transition metal dichalcogenides: from monolayer to bulk, *npj 2D Mater. Appl.* **2**, 6 (2018).
- [75] X. L. Yang, S. H. Guo, F. T. Chan, K. W. Wong, and W. Y. Ching, Analytic solution of a two-dimensional hydrogen atom. I. nonrelativistic theory, *Phys. Rev. A* **43**, 1186 (1991).